Mechanical mapping of spinal cord development and repair in living zebrafish larvae using Brillouin microscopy

Raimund Schlüßler[1,*,+], Stephanie Möllmert[1,+], Shada Abuhattum[1], Conrad Möckel[1], Conrad Zimmermann[1], Jürgen Czarske[2], and Jochen Guck[1,]**

[1]Biotechnology Center, Center for Molecular and Cellular Bioengineering, Technische Universität Dresden, Dresden, Germany
[2]Laboratory of Measurement and Sensor System Technique, Technische Universität Dresden, Dresden, Germany
[*]raimund.schluessler@tu-dresden.de
[**]jochen.guck@tu-dresden.de
[+]these authors contributed equally to this work

ABSTRACT

The mechanical properties of biological tissues are increasingly recognized as important in developmental and pathological processes. Most existing mechanical measurement techniques either necessitate destruction of the tissue for access or provide insufficient spatial resolution. Here, we show for the first time a systematic application of confocal Brillouin microscopy to quantitatively map the mechanical properties of spinal cord tissues during biologically relevant processes in a contact-free and non-destructive manner. Living zebrafish larvae were mechanically imaged in all anatomical planes, during development and after spinal cord injury. These experiments revealed that Brillouin microscopy is capable of detecting the mechanical properties of distinct anatomical structures without interfering with the animal's natural development. The Brillouin shift within the spinal cord increased during development and transiently decreased during the repair processes following spinal cord transection. These results show that the larval zebrafish spinal cord tissue presents mechanical signals for mechanosensitive cells residing in the tissue. The work presented constitutes the first step towards an *in vivo* assessment of spinal cord tissue mechanics during regeneration, provides a methodical basis to identify key determinants of mechanical tissue properties and allows to test their relative importance in combination with biochemical and genetic factors during developmental and regenerative processes.

Introduction

In response to a mechanical stimulus, many cell types, including neurons and glia, change their properties and behavior[1–5]. This includes morphological changes[6–8] as well as alterations of migration[9], proliferation[10] and differentiation[7]. The cellular susceptibility to mechanical signals is termed mechanosensitivity and has been the subject of recent studies documenting the involvement of mechanical signals in developmental and pathological processes. Axonal growth during optic tract development in *Xenopus laevis*, for instance, is guided by temporally changing stiffness gradients in adjacent brain tissue[11]. Microglial cells and astrocytes in rat brains display an activated phenotype and increase expression of inflammatory genes and proteins, which is indicative of reactive gliosis, when exposed to a mechanical stimulus that deviates from their physiological mechanical environment[12]. Oligodendrocyte precursor cells increase their expression of myelin basic protein and display an elaborated myelin membrane on stiffer substrates as compared to more compliant substrates indicating a preferred mechanical environment for differentiation[7]. Among others, these examples demonstrate an intricate interplay between the mechanosensitivity of distinct neural cell types and the mechanical properties of their respective microenvironments. *In vivo*, these microenvironments are formed by the surrounding nervous tissue whose mechanical properties are thought to be determined by the combined material properties of neighboring cells, extra cellular matrix and the degree of cross-linking[13]. As these determinants of tissue mechanics change during development and after pathological events, concomitant changes of mechanical tissue properties and their direct involvement in a wide range of CNS conditions and diseases are likely[14–17].

Severe injury to the mammalian spinal cord prompts a biochemical signaling cascade that eventually leads to the formation of a glial-fibrotic scar. The scar tissue has not only been shown to prevent axonal regrowth across the lesion site due to its biochemical composition[18,19], but has also been proposed to act as a mechanical obstacle[19,20]. Unlike mammalian systems, in which the loss of motor and sensory function associated with traumatic spinal cord injury is permanent, zebrafish are able to restore motor function and repair spinal cord tissue even after complete spinal cord transection[21]. In adult

zebrafish, functional recovery correlates with an orchestrated cellular response that includes proliferation[22–25], migration[23,25,26], differentiation[22,25,27] and morphological changes[22,23]. Radial glial cell, for example, proliferate and give rise to new motor neurons that mature and integrate into the spinal circuitry[22]. Descending axonal projections severed by the injury initiate regrowth and eventually traverse the injury site[25,28]. These regenerative events take place in a time interval of approximately six to eight weeks post-injury[22,25]. Larval zebrafish have been shown to share the regenerative capacity with their adult counterparts, as they too respond to spinal cord transection by proliferation, neurogenesis, axonal regrowth and functional recovery[29–32], yet with a much shorter recovery time[29,31,33].

In light of the aforementioned examples of neural mechanosensitivity and stiffness changes of nervous tissue during development and disease, we submit that the mechanical characterization of zebrafish spinal cord tissue poses an intriguing addition to biochemical analysis and might help to elucidate the role of mechanical signaling during spinal cord development and successful spinal cord repair.

To quantify the mechanical properties of biological samples, a variety of standard measurement techniques has been developed[34]. However, only a fraction of these techniques is suitable for probing the mechanics of native tissues[35]. These include e.g. AFM-based indentation[36–38] or sonoelastography and magnetic resonance elastography (MRE)[39]. While the former necessitates direct physical contact between indenter and sample and can therefore only measure at a surface and necessitates tissue destruction to access interior areas, the latter lack spatial resolution in the range relevant for cellular mechanosensitivity and required for samples with small dimensions e.g. zebrafish larvae.

Brillouin spectroscopy allows measurements of mechanical properties and is widely used in the material sciences. The technique is based on the inelastic Brillouin scattering process between incident photons and mass density fluctuations (acoustic phonons) due to inherent, travelling sound waves in the sample (see. Methods)[40,41]. It gives access to the phonon's properties which are related to the viscoelasticity of the sample, e.g. the longitudinal modulus and the loss modulus. With the emergence of virtually imaged phased array (VIPA) based spectrometers in the last decade, this technique has become applicable for the point-wise measurement within living biological samples to build up a three-dimensional image with diffraction-limited resolution[42]. Brillouin microscopy has so far been applied to human cornea[43–45], murine carotid arteries[46], ruminant retina[47], rabbit bone tissue[48] and zebrafish embryos[49–51]. Here, we exploit the optical transparency and high regenerative capacity of zebrafish larvae to systematically explore the *in vivo* mechanical properties of larval tissue during development and repair using a custom-built Brillouin microscopy setup.

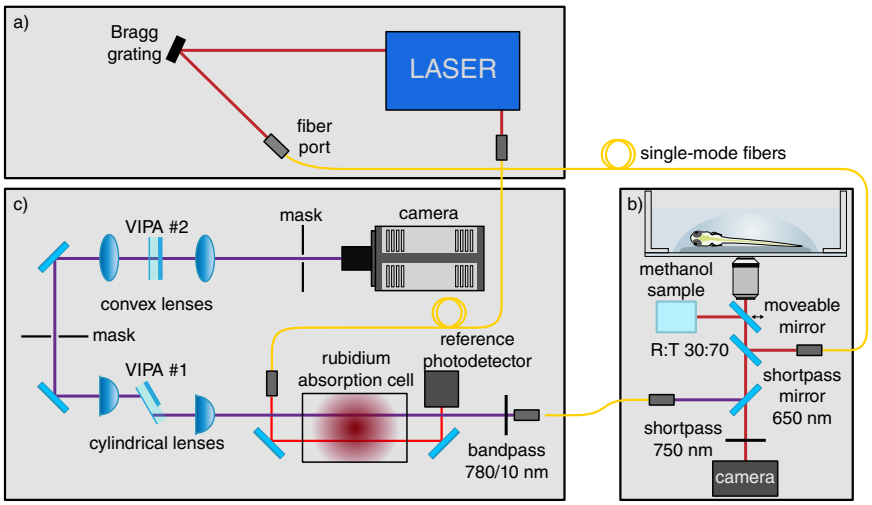

Figure 1. Scheme of the custom-built confocal Brillouin microscope. The setup consists of a) a diode laser to illuminate the specimen, b) a confocal microscope and c) the Brillouin spectrometer. The light elastically scattered in the specimen is collected in backscattering direction and coupled into a two-stage VIPA spectrometer including a molecular absorption cell filled with Rubidium. The spectrogram is acquired with an sCMOS-camera and evaluated using a self written MATLAB program.

Our Brillouin microscope (Fig. 1) is based on a two-stage VIPA interferometer design from Scarcelli et. al.[42,52–54]. As illumination source we use a frequency modulated diode laser (Toptica DLC TA PRO 780) emitting at 780.24 nm whose central frequency is stabilized to the D_2 transition of rubidium ^{85}Rb. For this purpose, a probe beam from the laser is transmitted through a Rb molecular absorption cell. The intensity behind the cell is measured by a reference photodetector and used as input signal for the lock-in frequency stabilization. The laser spectrum is cleaned using a Bragg grating (Ondax NoiseBlock) to

increase the laser mode to amplified spontaneous emission (ASE) ratio by 10 dB to over 65 dB. The laser light is then coupled into a single-mode fiber and guided to a custom-built inverse confocal microscope. The confocal microscope is based on a Zeiss Axiovert 200M microscope stand equipped with a translation stage. The light emitted from the illumination fiber is collimated, guided to the objective and focused into the specimen with a total power of 10 mW in the sample. Alternatively, a moveable mirror can be shifted into the beam path guiding the light to a methanol-filled cuvette used as calibration sample. To achieve a sufficient working distance, a Plan Neofluar 20x/0.5 objective is used, which results in a subcellular spatial resolution of 2 µm in the lateral plane and approximately 6 µm in the axial direction. The sample is furthermore illuminated with a white light source to acquire a brightfield image after the Brillouin measurement. The Brillouin scattered light is collected in backscattering direction and separated from the brightfield illumination by a shortpass mirror (Thorlabs DMSP650) with 650 nm cut-off wavelength. To achieve confocality, a second single-mode fiber guiding the light into the Brillouin spectrometer is used. In the spectrometer, the light is collimated and subsequently filtered by a band-pass (Thorlabs FBH780-10) to block Raman scattered light. The molecular absorption cell (Precision Glass Blowing TG-ABRB-I85-Q) absorbs light with the same frequency as the excitation laser (eg. Rayleigh scattered and reflected light)[55]. After passing the absorption cell, the beam is guided to two VIPA interferometers (Light machinery OP-6721-6743-4) with 15 GHz free spectral range. The interferometers lead to an angular dispersion of light with different frequencies[53], which allows to image the Brillouin spectrum of the probed measurement point on the sCMOS camera (Andor Zyla 4.2 PLUS). For this purpose, an acquisition time of 500 ms per spectrum is used, which we found optimal in order to minimize the measurement uncertainty, and two spectra per measurement point are recorded. By translating the specimen, a spatially resolved map of the Brillouin shift is acquired.

The obtained Brillouin images show the different viscoelastic properties of varying anatomical structures within living zebrafish larvae. We furthermore show that the Brillouin shift of the spinal cord increases during development. After spinal cord injury, we detect a significant, but transient drop of the Brillouin shift at the lesion site. Thus, our experiments show for the first time that zebrafish spinal cord tissue, mechanically mapped inside living and intact animals, presents distinct mechanical signals to mechanosensitive cells during development and regeneration. This work constitutes the methodical basis to identify key determinants of mechanical central nervous system tissue properties and to test the relative importance of mechanics in combination with biochemical and genetic factors during biologically important processes in vivo.

Results

Brillouin microscopy mechanically characterizes anatomical structures in living zebrafish larvae

To identify anatomical structures and assign viscoelastic properties to distinct organs and tissues in the living zebrafish larva, we compared images acquired with Brillouin microscopy with images from brightfield and confocal fluorescence microscopy of the same specimens (Fig. 2). For this purpose, individual four-day-old zebrafish larvae were anesthetized and immobilized using low gelling point agarose in a glass bottom dish suitable for optical imaging. Using Brillouin microscopy, we measured the mechanical properties of the larval tissues in all three anatomical planes. All specimens were subsequently imaged using brightfield microscopy, and fixed and stained with TRITC-conjugated phalloidin and DAPI for confocal fluorescence microscopy. While the formation of melanophores could be suppressed successfully, all zebrafish exhibited the two other types of pigment cells, xanthophores and iridophores. The latter can be observed as dark spots in all brightfield images (Fig. 2a,b) and caused reflections in the Brillouin images (Fig. 2d,e,f). The corresponding values were therefore discarded and displayed as white pixels in the Brillouin images.

In both the brightfield images (Fig. 2a,b) and the Brillouin peak intensity map (Fig. 2d), image contrast is governed by absorption and scattering processes in the specimen, which allows to discern prominent anatomical structures such as the notochord and the diagonal pattern of the muscle segments. The fluorescence image (Fig. 2c) allows additionally to distinguish the spinal cord tissue (blue) from the surrounding muscle tissue (red). While the aforementioned imaging modalities convey information about the presence of certain anatomical features, the Brillouin shift and the linewidth (FWHM) show the mechanical properties of these features. The Brillouin peak linewidth depends on the phonon lifetime and is therefore directly related to the loss modulus and the viscosity of the sample (see Eq. [2]). The Brillouin peak linewidth (Fig. 2e) of the muscle tissue and the spinal cord displays a higher linewidth as compared to the linewidth of the intestinal tissue and the notochord. The Brillouin shift depends on the longitudinal modulus and is indicative of the elastic, solid-like sample properties (see Eq. [1]). Our measurements (Fig. 2f) revealed a higher Brillouin shift of the yolk extension, the muscle and spinal cord tissue as compared to the notochord. The Brillouin shift map also revealed the diagonal pattern of the muscle segments and we were able to detect the fins in the *yz*-plane. After the measurements the larvae were released from the agarose and behaved normally after cessation of sedation.

Brillouin shifts of the larval zebrafish spinal cord increase during development and decrease after injury

To detect changes of the mechanical properties of the spinal cord tissue during development, we probed the same specimens ($n = 6$) on three consecutive days. This allowed us to follow the evolution of the developmental mechanical phenotype that

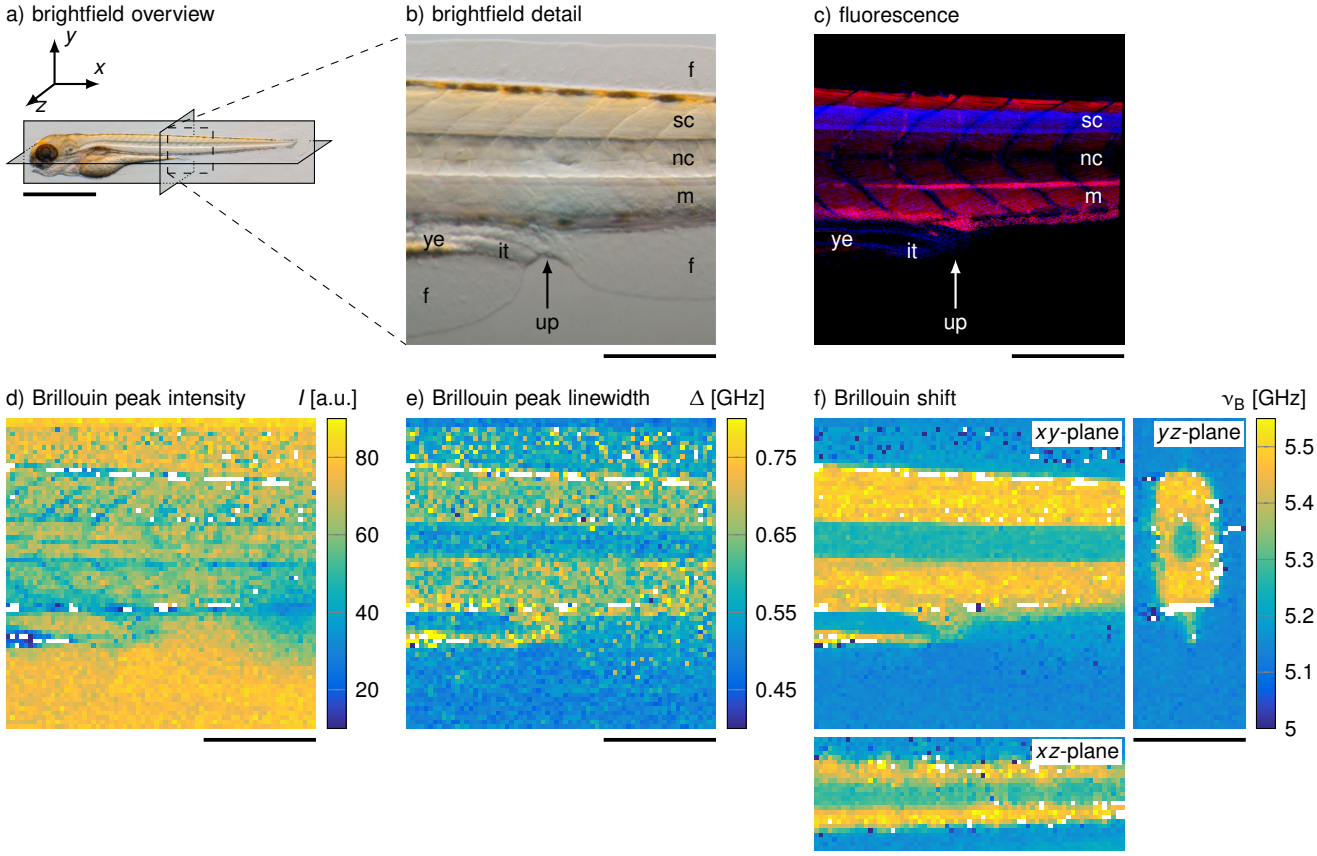

Figure 2. Images of the same zebrafish larva at four days post-fertilization (dpf). Brightfield and Brillouin images were obtained in a living specimen, fluorescence microscopy was performed after fixation following Brillouin microscopy. a) Brightfield image showing the specimen and the three anatomical planes. Scale bar, 1 mm. b) Enlarged brightfield image of the region of interest containing the spinal cord (sc), the notochord (nc), muscle segments (m), the fins (f), the yolk extension (ye), the intestinal tissue (it) and the urogenital pore (up). c) Corresponding fluorescence image depicting the same structures – spinal cord (DAPI, blue), muscle tissue (phalloidin-TRITC, red) and the notochord. Brillouin microscopy yields d) the peak intensity, e) the peak linewidth given as full width at half maximum (FWHM) and f) the Brillouin shift. The peak intensity detects anatomical structures that scatter or absorb light in the beam path. The peak width is indicative of the viscous properties. The Brillouin shift is displayed for the three anatomical planes indicated in a) and is proportional to the elastic properties of the sample. Scale bars b) – f), 200 µm.

might serve as a signaling cue for neurons and glial cells residing in the tissue. Both the brightfield image (Fig. 3a) and the Brillouin peak intensity map (Fig. 3b) display the position of the spinal cord, notochord and the regular diagonal pattern of the muscle tissue. The position and contrast of these structures remained similar during the investigated time interval, whereas the Brillouin shift (Fig. 3c) of the spinal cord tissue increased from 3 dpf to 5 dpf.

To test the hypothesis that the regenerating zebrafish spinal cord changes its mechanical properties and thereby provides mechanical cues during regeneration, we acquired Brillouin images after spinal cord transection until 2 days post-injury (Fig. 4). All specimens ($n = 6$) were imaged immediately before the injury at 3 dpf, 1 h after the injury (3^+ dpf) and on the two consecutive days (4 dpf and 5 dpf). The disrupted structure of the lesioned spinal cord is visible in both the brightfield image (Fig. 4a) and the Brillouin peak intensity map (Fig. 4b) where the lesion site displays lower values as compared to neighboring spinal cord tissue. Similarly, the map of the Brillouin shift (Fig. 4c) showed lower values in the lesion site than in the surrounding tissue parts. As the repair of spinal cord progressed, the Brillouin shift increased gradually.

The investigated time interval of lesioned animals coincided with the investigated developmental period of uninjured animals and therefore allowed for direct comparison. To quantify the change of the Brillouin shift, we averaged the Brillouin shift values for three selected regions. The regions of interest in the uninjured animals correspond to the entire spinal cord tissues (Fig. 5a, red box). For the lesioned fish, the spinal cord tissues were divided into regions containing the lesion site (Fig. 5a, blue box) and regions for the remaining tissues (Fig. 5a, green box). The increase of the Brillouin shifts in uninjured

animals from 3 dpf to 5 dpf (Fig. 5b) was significant ($p = 0.0043$). Brillouin shifts obtained from larvae after SCI showed the same trend at regions next to the lesion site (Fig. 5c). The lesion site itself (Fig. 5d) displayed a significant decrease of Brillouin shifts immediately after SCI ($p = 0.0087$) which recovered to levels prior to the injury within the following two days. However, Brillouin shifts of the injured site at two days post-injury (5 dpf) did not reach levels next to the injury site, nor the levels of uninjured specimens of the same age ($p = 0.0087$).

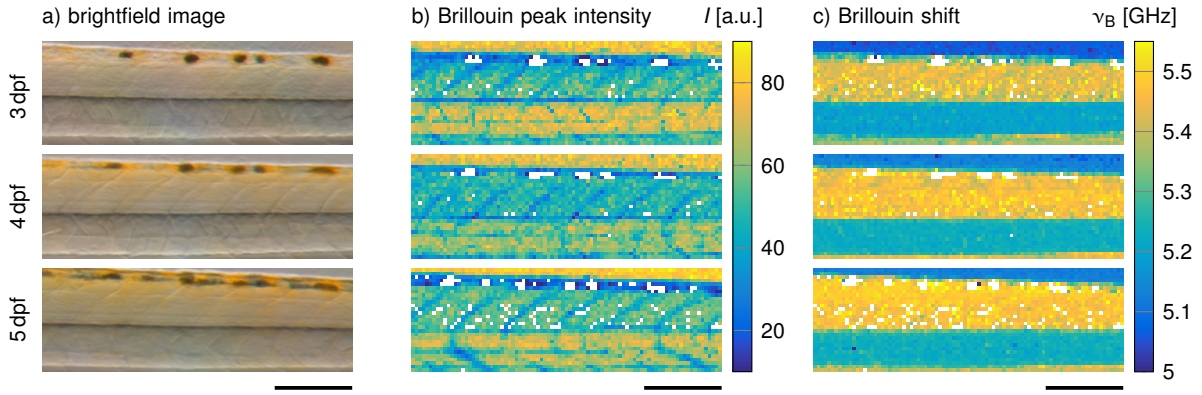

Figure 3. Brillouin measurements of a representative zebrafish larva during development. a) Brightfield images obtained directly after the Brillouin measurements. b) Corresponding peak intensities and c) Brillouin shifts of the same specimen. Scale bars, 150 µm.

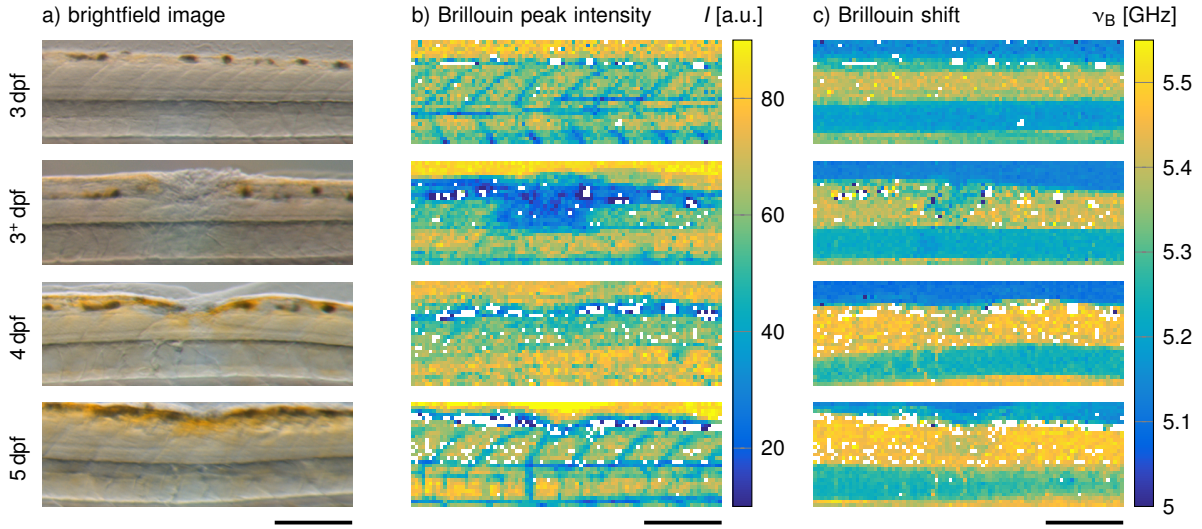

Figure 4. Brillouin measurements of a representative zebrafish larva after spinal cord injury. Lesioned larvae were probed at 3 dpf immediately before and 1 h after the injury (3^+ dpf) as well as on the two subsequent days (4 dpf and 5 dpf). a) Brightfield images obtained directly after the Brillouin measurements. b) Corresponding peak intensities and c) Brillouin shifts of the same specimen. Scale bars, 150 µm.

A decrease of Brillouin shifts coincides with lower cell body densities

The mechanical properties of nervous tissues have been correlated to local cell body density and distribution using the presence of nuclei as a proxy for cell bodies[11,37,47]. To investigate if the changes of Brillouin shifts observed in the present study coincide with an altered tissue structure and cell body arrangement, we fixed and stained uninjured and lesioned zebrafish after Brillouin microscopy (Fig. 6). Uninjured spinal cord tissue displayed a packing of cell nuclei that was translationally invariant along the anterior-posterior axis of the spinal cord. This highly ordered arrangement corresponded to evenly distributed Brillouin shifts. As described above, the lesion site displayed significantly decreased Brillouin shifts in comparison to uninjured animals. The low values in the lesion site corresponded to a disorganized arrangement of cell nuclei and a lower fluorescence intensity of the DAPI signal as compared to neighboring, structurally intact tissue segments.

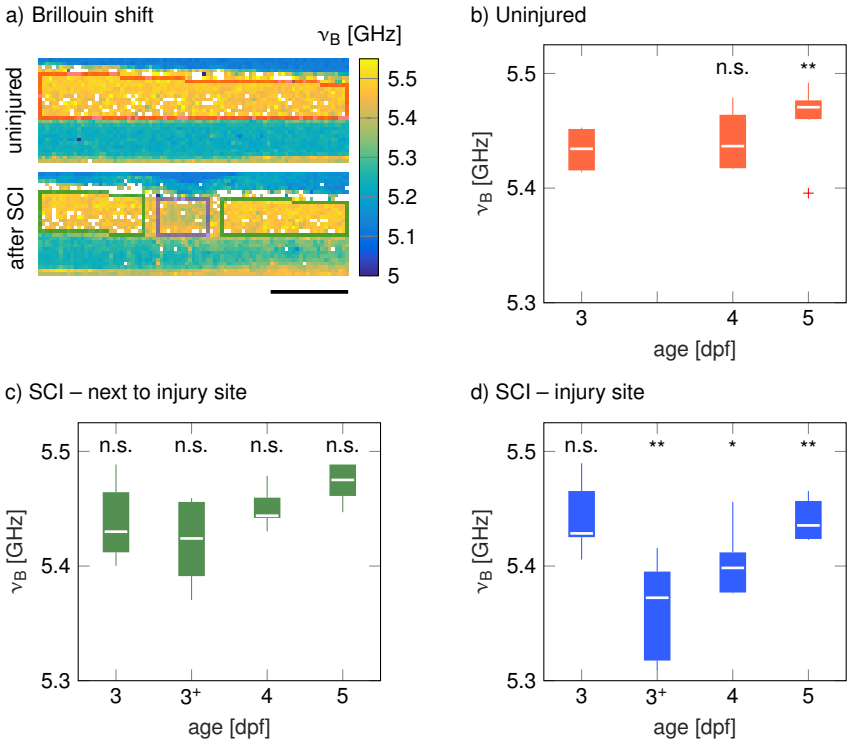

Figure 5. Quantification of the temporal development of the Brillouin shift during development and repair. a) The selected region of interest in the uninjured zebrafish ($n = 6$) comprises the complete spinal cord tissues (red box). For lesioned zebrafish ($n = 6$), the spinal cord tissue was divided into a region containing the lesion site (blue box) and a region for the remaining tissue (green box). Scale bar, 150 µm. b) – d) Box plots of the average Brillouin shifts of the respective areas in individual fish. Significance levels shown in b) refer to pairwise comparisons with 3 dpf. Indicated significant levels in c) and d) refer to pairwise comparisons of respective time points with uninjured animals in b). Brillouin shifts measured 1 h after spinal cord injury (3^+ dpf) were also compared to 3 dpf values from uninjured specimens. $^*p < 0.05$; $^{**}p < 0.01$.

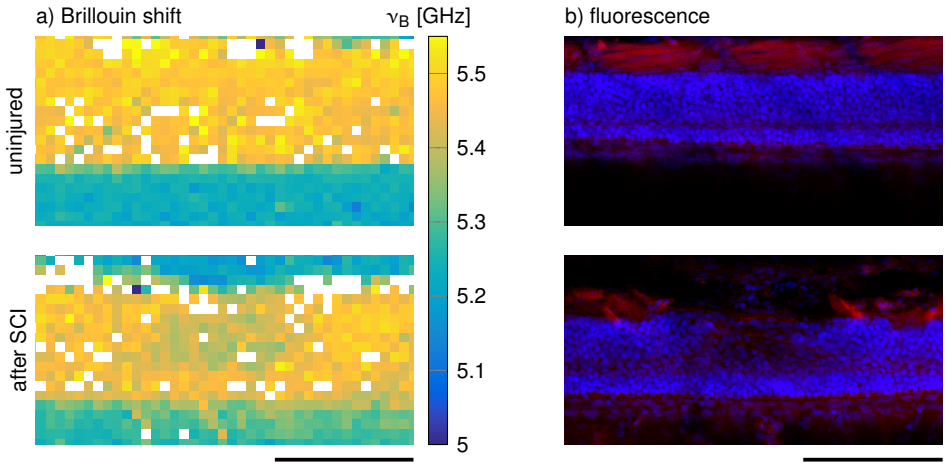

Figure 6. Comparison of a) the Brillouin shift and b) the corresponding fluorescence image for an uninjured and a lesioned zebrafish spinal cord at 5 dpf. The fluorescence image shows cell nuclei (DAPI, blue) and actin filaments (phalloidin-TRITC, red). Scale bars, 100 µm.

Discussion

In this report, we demonstrated the first systematic investigation of the mechanical properties of larval tissues in living zebrafish. By using our confocal Brillouin microscopy setup, we were able to determine the mechanical phenotypes of distinct anatomical structures. The measurements show a lower Brillouin shift and a lower Brillouin peak linewidth of the notochord as compared to the spinal cord and muscle tissue. This conforms with a previous study characterizing the notochord as a fluid-filled structure[56]. As for the yolk extension, we found similar values as previously reported for zebrafish embryos[51]. Our results furthermore showed that developmental and pathological processes of larval zebrafish spinal cords coincide with significant Brillouin shift changes. During development, we detected an increase of the Brillouin shifts. After injury, the Brillouin shifts measured in the lesion site decreased immediately, but gradually increased thereafter. Spinal cord injured zebrafish also displayed a disorganized arrangement and a lower number of cell nuclei at the lesion site. These observations are in agreement with previous studies on mammals, showing that CNS tissue stiffness scales with cell body density[11,37,47,57]. Our results might therefore indicate that cell body density also contributes to the mechanical properties of the spinal cord tissue in larval zebrafish.

The Brillouin shift scales with the longitudinal modulus, the refractive index and the mass density of the sample (see Eq. [1]). Using the current setup, it is not possible to quantitatively distinguish between changes of these properties. However, refractive index and mass density are directly coupled for biological materials[58–62], which renders the Brillouin shift dependent solely on the mechanical properties (i.e. the longitudinal modulus and the mass density) of the sample. Furthermore, this relation allows to calculate the longitudinal modulus in case the Brillouin shift and the refractive index are known. Recent advances in refractive index tomography enable to measure the three-dimensional refractive index distribution[62,63]. Hence, by combining refractive index tomography and Brillouin microscopy, an unambiguous distribution of the mass density and the elastic and viscous properties could be obtained.

While e.g. AFM gives direct access to the elastic modulus by mechanically probing, it requires access to surfaces, and, thus, cutting the sample. The cutting can lead to cell death, relieve of tension and hydrostatic pressure, lack of neighboring cells, etc., which can all lead to changes in the mechanical properties measured. Since Brillouin microscopy is a non-invasive technique, neither cutting nor special sample preparations are necessary and three-dimensional measurements of the mechanical properties of living tissues are possible. Also, liquid-filled structures as the notochord can be characterized. Furthermore, in comparison to other non-invasive techniques such as MRE, Brillouin microscopy achieves sub-cellular spatial resolution, which allows to resolve the mechanical properties of structures within the spinal cords of zebrafish larvae.

The changes of the mechanical properties observed in the larval zebrafish may serve as signaling cues for mechanosensitive neural cell types residing in the spinal cord tissue. In fact, the functional recovery of zebrafish after injury, and the lack thereof in mammals, is associated with cell types and cellular processes that are mechanosensitive both *in vitro* and *in vivo*. This work constitutes the methodical basis to identify key determinants of mechanical central nervous system tissue properties and to test the relative importance of mechanics in combination with biochemical and genetic factors during biologically important processes *in vivo*. Future insights into the mechanical mechanisms promoting or inhibiting neuronal regrowth, enabled by Brillouin microscopy as demonstrated in this study, might therefore constitute important additions to biochemical, or cell and molecular biological analyses, and could eventually even provide novel therapeutic strategies for affected humans.

Methods

Animals

All zebrafish were kept and bred in the fish facility of BIOTEC, TU Dresden as described in[64]. Embryos from wild-type (WIK) zebrafish were incubated in PTU (1-phenyl-2-thiourea, Sigma-Aldrich, 0.003 75 % in E3 embryo medium) after 24 hpf to prevent melanogenesis[65].

Mounting for Brillouin and brightfield imaging

Larvae were anesthetized in MS222 (0.01 % in E3, Sigma-Aldrich) and placed in a lateral position on a 30 µm thick, flat polyacrylamide (PAA) gel that had been polymerized on a glass bottom dish suitable for optical imaging. A drop (200 µl) of low gelling point agarose (1 % in E3, 30 °C, Sigma-Aldrich) was used to immobilize the larvae in this position for subsequent imaging. Immobilized larvae were then immersed in MS222 (0.01 % in E3) during imaging. All specimens were released from the agarose embedding between Brillouin measurements and kept under standard conditions[64].

Fluorescence microscopy

After obtaining the final Brillouin image, zebrafish larvae were sacrificed by an overdose of MS222, fixed with PFA (4 % in PBS), subjected to multiple washing and permeabilization steps using PBSTx (0.8 % TritonX-100, 1 % DMSO in PBS) and stained with DAPI and phalloidin-TRITC (both 1:1000 in PBS). Larvae were then washed with PBS, incubated in glycerol (75 % in PBS) for 3 h and mounted in DABCO containing mounting medium (2.5 % DABCO, Sigma-Aldrich, 90 % in PBS in 50 mM Tris-HCl, pH 8).

Image acquisition and processing

Brightfield images were obtained using the Olympus Stereomicroscope SZX 16 and the SDF PLAPO 0.8x/0.12 and 2.0x/0.3 objectives. Confocal fluorescence microscopy was performed to image fixed and stained larvae using the Zeiss LSM700 and a Plan Apochromat 10x/0.45 objective. The fluorescence images displayed in this study are maximum z-projections of four optical sections ($\approx 1\,\mu m$ each) which correlates to the section thickness measured by Brillouin microscopy. Brightfield and fluorescence images were adjusted in brightness and contrast using Fiji and assembled with CorelDraw.

Spinal cord lesion

Larvae were anesthetized in MS222 (0.01 % in E3) and immobilized as described for Brillouin imaging. Lesions were performed manually at 3 dpf by inserting the broken tip of a pulled injection glass capillary in the most ventral part of the spinal cord at the level of the urogenital pore, and moving the tip dorsally in a quick motion. Notochords and major blood vessels remained intact. Larvae were subsequently released from the agarose embedding.

Brillouin scattering

Brillouin scattering is an inelastic scattering process between the incident light and periodic mass density fluctuations due to travelling sound waves with sound velocity V within the sample. This results in an upward and downward frequency shift ν_B (i.e. Brillouin shift) of the incident light, which is given by[41,66]

$$\nu_B = \frac{2\cos(\Theta/2)}{\lambda} \cdot n \cdot V = \zeta \cdot \sqrt{M'} \qquad \text{with} \qquad \zeta = \frac{2\cos(\Theta/2)}{\lambda} \cdot \frac{n}{\sqrt{\rho}} \qquad [1]$$

where Θ is the scattering angle and λ the wavelength. The mechanical properties of the sample are described by the longitudinal modulus M', the refractive index n and the mass density ρ of which the refractive index and the mass density are directly coupled for most biological samples[58–62]. The linewidth Δ (full-width at half maximum) of the Brillouin peak is given by[67,68]

$$\Delta = \zeta^2 \cdot \frac{M''}{\nu_B} = 2\pi\zeta^2 \cdot \eta \qquad [2]$$

where M'' is the loss modulus and η the viscosity.

Brillouin imaging

The acquisition of the camera images as well as the control of the translation stage and the objective lens' z-position are performed using a custom MATLAB program. The acquired raw data is stored as HDF5 file allowing for efficient data handling[69]. The subsequent data analysis also uses a custom MATLAB program and is done in multiple steps. First, the one-dimensional Brillouin spectra are extracted from the two-dimensional camera images. The position, width and intensity of the Brillouin and Rayleigh peaks are then determined by fitting Lorentzian functions to every peak. In order to calibrate the frequency axis, a reference measurement of a methanol sample placed in the calibration beam path is acquired every 10 min by moving a mirror into the beam path. This allows to obtain an absolute value for the Brillouin shift and compensates for possible drifts of the VIPA setup during the measurement. For every reference measurement we fit the theoretical, non-linear frequency axis to the Brillouin spectrum according to[70]. By interpolating along the temporal axis we then get a calibrated frequency axis for every time point during the measurement, which is used to calculate the Brillouin shift in GHz. Plotting the calibrated Brillouin shift over the position of the translation stage finally leads to a spatially resolved map of the mechanical properties of the sample. All white pixels displayed in the maps correspond to coordinates in which the sample caused strong reflections. These values were discarded.

Statistical analysis

To compare the Brillouin shifts of different regions within the specimens' spinal cords, the values corresponding to every region had to be identified. For this purpose, all measurement points belonging to the specimen's spinal cord were selected first. For the injury site, all values in the spinal cord in an area with a width of $100\,\mu m$ around the center of the lesion were chosen. The region next to the injury site included all values in the spinal cord separated from the injury site by a $25\,\mu m$ clearance to exclude the transient values between both regions. All Brillouin shifts corresponding to the identified regions were averaged for the individual specimen, yielding $n = 6$ mean values for every region and for the injured and uninjured zebrafish, respectively. The mean values were subjected to statistical analysis by the two-tailed Mann-Whitney U-test using MATLAB and printed as boxplots. The shown asterisks indicate the significance levels: $^{*}p < 0.05$ and $^{**}p < 0.01$.

References

1. Engler, A. J., Sen, S., Sweeney, H. L. & Discher, D. E. Matrix elasticity directs stem cell lineage specification. *Cell* **126**, 677–689 (2006).
2. Mendez, M. G. & Janmey, P. A. Transcription factor regulation by mechanical stress. *Int. J. Biochem. Cell Biol.* **44**, 728–732 (2012).
3. Roca-Cusachs, P., Sunyer, R. & Trepat, X. Mechanical guidance of cell migration: lessons from chemotaxis. *Curr. Opin. Cell Biol.* **25**, 543–549 (2013).
4. Klein, E. A. *et al.* Cell-cycle control by physiological matrix elasticity and *in vivo* tissue stiffening. *Curr. Biol.* **19**, 1511–1518 (2009).
5. Franze, K., Janmey, P. A. & Guck, J. Mechanics in neuronal development and repair. *Annu. Rev. Biomed. Eng.* **15**, 227–251 (2013).
6. Flanagan, L. A., Ju, Y. E., Marg, B., Osterfield, M. & Janmey, P. A. Neurite branching on deformable substrates. *Neuroreport* **13**, 2411–2415 (2002).
7. Jagielska, A. *et al.* Mechanical environment modulates biological properties of oligodendrocyte progenitor cells. *Stem Cells Dev.* **21**, 2905–2914 (2012).
8. Moshayedi, P. *et al.* Mechanosensitivity of astrocytes on optimized polyacrylamide gels analyzed by quantitative morphometry. *J. Phys. Condens. Matter* **22**, 194114 (2010).
9. Lo, C. M., Wang, H. B., Dembo, M. & Wang, Y. L. Cell movement is guided by the rigidity of the substrate. *Biophys. J.* **79**, 144–152 (2000).
10. Ulrich, T., de Juan Pardo, E. & Kumar, S. The mechanical rigidity of the extracellular matrix regulates the structure, motility, and proliferation of glioma cells. *Cancer Res.* **69**, 4167–4174 (2009).
11. Koser, D. E. *et al.* Mechanosensing is critical for axon growth in the developing brain. *Nat. Neurosci.* **19**, 1592–1598 (2016).
12. Moshayedi, P. *et al.* The relationship between glial cell mechanosensitivity and foreign body reactions in the central nervous system. *Biomater.* **35**, 3919–3925 (2014).
13. Lu, Y. B. *et al.* Viscoelastic properties of individual glial cells and neurons in the CNS. *Proc. Natl. Acad. Sci. U. S. A.* **103**, 17759–17764 (2006).
14. Iwashita, M., Kataoka, N., Toida, K. & Kosodo, Y. Systematic profiling of spatiotemporal tissue and cellular stiffness in the developing brain. *Dev.* **141**, 3793–3798 (2014).
15. Sack, I., Jöhrens, K., Würfel, J. & Braun, J. Structure-sensitive elastography: on the viscoelastic powerlaw behavior of *in vivo* human tissue in health and disease. *Soft Matter* **9**, 5672–5680 (2013).
16. Millward, J. M. *et al.* Tissue structure and inflammatory processes shape viscoelastic properties of the mouse brain. *NMR Biomed.* **28**, 831–839 (2015).
17. Moeendarbary, E. *et al.* The soft mechanical signature of glial scars in the central nervous system. *Nat. Commun.* **8**, 14787 (2017).
18. Silver, J., Schwab, M. E. & Popovich, P. G. Central nervous system regenerative failure: Role of oligodendrocytes, astrocytes, and microglia. *Cold Spring Harb. Perspectives Biol.* **7** (2015).
19. Silver, J. & Miller, J. H. Regeneration beyond the glial scar. *Nat. Rev. Neurosci.* **5**, 146–156 (2004).
20. Fawcett, J. W. & Asher, R. A. The glial scar and central nervous system repair. *Brain Res. Bull.* **49**, 377–391 (1999).
21. Becker, C. G. & Becker, T. Adult zebrafish as a model for successful central nervous system regeneration. *Restor. Neurol. Neurosci.* **26**, 71–80 (2008).
22. Reimer, M. M. *et al.* Motor neuron regeneration in adult zebrafish. *J. Neurosci.* **28**, 8510–8516 (2008).
23. Goldshmit, Y. *et al.* Fgf-dependent glial cell bridges facilitate spinal cord regeneration in zebrafish. *J. Neurosci.* **32**, 7477–7492 (2012).
24. Hui, S. P., Nag, T. C. & Ghosh, S. Characterization of proliferating neural progenitors after spinal cord injury in adult zebrafish. *PLoS ONE* **10**, e0143595 (2015).
25. Hui, S. P., Dutta, A. & Ghosh, S. Cellular response after crush injury in adult zebrafish spinal cord. *Dev. Dyn.* **239**, 2962–2979 (2010).

26. Becker, T. & Becker, C. G. Regenerating descending axons preferentially reroute to the gray matter in the presence of a general macrophage/microglial reaction caudal to a spinal transection in adult zebrafish. *J. Comp. Neurol.* **433**, 131–147 (2001).

27. Kuscha, V. *et al.* Lesion-induced generation of interneuron cell types in specific dorsoventral domains in the spinal cord of adult zebrafish. *J. Comp. Neurol.* **520**, 3604–3616 (2012).

28. Becker, T., Wullimann, M. F., Becker, C. G., Bernhardt, R. R. & Schachner, M. Axonal regrowth after spinal cord transection in adult zebrafish. *J. Comp. Neurol.* **377**, 577–595 (1997).

29. Briona, L. K. & Dorsky, R. I. Radial glial progenitors repair the zebrafish spinal cord following transection. *Exp. Neurol.* **256**, 81–92 (2014).

30. Briona, L. K., Poulain, F. E., Mosimann, C. & Dorsky, R. I. Wnt/ss-catenin signaling is required for radial glial neurogenesis following spinal cord injury. *Dev. Biol.* **403**, 15–21 (2015).

31. Ohnmacht, J. *et al.* Spinal motor neurons are regenerated after mechanical lesion and genetic ablation in larval zebrafish. *Dev.* **143**, 1464–1474 (2016).

32. Mokalled, M. H. *et al.* Injury-induced *ctgfa* directs glial bridging and spinal cord regeneration in zebrafish. *Sci.* **354**, 630–634 (2016).

33. Wehner, D. *et al.* Wnt signaling controls pro-regenerative collagen XII in functional spinal cord regeneration in zebrafish. *Nature. Commun.* **8** (2017).

34. Addae-Mensah, K. A. & Wikswo, J. P. Measurement techniques for cellular biomechanics *in vitro*. *Exp. biology medicine (Maywood, N.J.)* **233**, 792–809 (2008).

35. Greenleaf, J. F., Fatemi, M. & Insana, M. Selected methods for imaging elastic properties of biological tissues. *Annu. Rev. Biomed. Eng.* **5**, 57–78 (2003).

36. Christ, A. F. *et al.* Mechanical difference between white and gray matter in the rat cerebellum measured by scanning force microscopy. *J. Biomech.* **43**, 2986 – 2992 (2010).

37. Koser, D., Moeendarbary, E., Hanne, J., Kuerten, S. & Franze, K. CNS cell distribution and axon orientation determine local spinal cord mechanical properties. *Biophys. J.* **108**, 2137 – 2147 (2015).

38. Gautier, H. O. *et al.* Atomic force microscopy-based force measurements on animal cells and tissues. *Methods Cell Biol.* **125**, 211 – 235 (2015).

39. Sarvazyan, A. *et al.* An overview of elastography – an emerging branch of medical imaging. *Curr. medical imaging reviews* **7**, 255–282 (2011).

40. Brillouin, L. Diffusion de la lumière et des rayons x par un corps transparent homogène - influence de l'agitation thermique. *Ann. Phys.* **9**, 88–122 (1922).

41. Boyd, R. W. *Nonlinear Optics* (Academic Press, 2008).

42. Scarcelli, G. & Yun, S. H. Confocal Brillouin microscopy for three-dimensional mechanical imaging. *Nature. Photonics* **2**, 39–43 (2008).

43. Scarcelli, G., Kim, P. & Yun, S. *In vivo* measurement of age-related stiffening in the crystalline lens by Brillouin optical microscopy. *Biophys. J.* **101**, 1539 – 1545 (2011).

44. Scarcelli, G. & Yun, S. H. *In vivo* Brillouin optical microscopy of the human eye. *Opt. Express* **20**, 9197–9202 (2012).

45. Scarcelli, G., Besner, S., Pineda, R. & Yun, S. H. Biomechanical characterization of keratoconus corneas *ex vivo* with Brillouin microscopy. *Investig. Ophthalmol. & Vis. Sci.* **55**, 4490 (2014).

46. Antonacci, G. *et al.* Quantification of plaque stiffness by Brillouin microscopy in experimental thin cap fibroatheroma. *J. The Royal Soc. Interface* **12** (2015).

47. Weber, I., Yun, S.-H., Scarcelli, G. & Franze, K. The role of cell body density in ruminant retina mechanics assessed by atomic force and Brillouin microscopy. *Phys. Biol.* (2017).

48. Mathieu, V. *et al.* Micro-Brillouin scattering measurements in mature and newly formed bone tissue surrounding an implant. *J. Biomech. Eng.* **133**, 021006–021006–6 (2011).

49. Fujimura, Y., Inoue, M., Kondoh, H. & Kinoshita, S. Measurement of micro-elasticity within a fertilized egg by using Brillouin scattering spectroscopy. *J. Korean Phys. Soc.* **51**, 854–857 (2007).

50. Meng, Z., Traverso, A. J., Ballmann, C. W., Troyanova-Wood, M. A. & Yakovlev, V. V. Seeing cells in a new light: a renaissance of Brillouin spectroscopy. *Adv. Opt. Photonics* **8** (2016).

51. Meng, Z., Hanson, J. A. & Yakovlev, V. V. Watching embryonic development in a new light: elasticity specific imaging with dual Brillouin/Raman microspectroscopy. In *Proc. SPIE 9716, Optical Methods in Developmental Biology IV*, vol. 9716, 97160L–97160L–6 (2016).

52. Scarcelli, G., Kim, P. & Yun, S. H. Cross-axis cascading of spectral dispersion. *Opt. Lett.* **33**, 2979–2981 (2008).

53. Scarcelli, G. & Yun, S. H. Multistage VIPA etalons for high-extinction parallel Brillouin spectroscopy. *Opt. Express* **19**, 10913–22 (2011).

54. Berghaus, K. V., Yun, S. H. & Scarcelli, G. High speed sub-GHz spectrometer for Brillouin scattering analysis. *J. Vis. Exp.* e53468 (2015).

55. Meng, Z., Traverso, A. J. & Yakovlev, V. V. Background clean-up in Brillouin microspectroscopy of scattering medium. *Opt. Express* **22**, 5410–5415 (2014).

56. Ellis, K., Bagwell, J. & Bagnat, M. Notochord vacuoles are lysosome-related organelles that function in axis and spine morphogenesis. *The J. Cell Biol.* **200**, 667–679 (2013).

57. Franze, K. *et al.* Spatial mapping of the mechanical properties of the living retina using scanning force microscopy. *Soft Matter* **7**, 3147–3154 (2011).

58. Barer, R. Interference microscopy and mass determination. *Nature.* **169**, 366–367 (1952).

59. Davies, H. G. & Wilkins, M. H. F. Interference microscopy and mass determination. *Nature.* **169**, 541–541 (1952).

60. Zangle, T. A. & Teitell, M. A. Live-cell mass profiling: an emerging approach in quantitative biophysics. *Nat Meth* **11**, 1221–1228 (2014).

61. Popescu, G. *et al.* Optical imaging of cell mass and growth dynamics. *Am. J. Physiol. - Cell Physiol.* **295**, C538–C544 (2008).

62. Schürmann, M., Scholze, J., Müller, P., Guck, J. & Chan, C. J. Cell nuclei have lower refractive index and mass density than cytoplasm. *J. Biophotonics* **9**, 1068–1076 (2016).

63. Kim, K., Choe, K., Park, I., Kim, P. & Park, Y. Holographic intravital microscopy for 2-D and 3-D imaging intact circulating blood cells in microcapillaries of live mice. *Sci. Reports* **6**, 33084 (2016).

64. Brand, M., Granato, M. & Nüsslein-Volhard, C. *Zebrafish - A Practical Approach*, chap. Keeping and raising zebrafish (Oxford University Press, Oxford, UK, 2002).

65. Karlsson, J., von Hofsten, J. & Olsson, P.-E. Generating transparent zebrafish: A refined method to improve detection of gene expression during embryonic development. *Mar. Biotechnol.* **3**, 522–527 (2001).

66. Dil, J. G. Brillouin scattering in condensed matter. *Reports on Prog. Phys.* **45**, 285 (1982).

67. Carroll, P. J. & Patterson, G. D. Rayleigh–Brillouin spectroscopy of simple viscoelastic liquids. *The J. Chem. Phys.* **81**, 1666–1675 (1984).

68. Dukhin, A. S. & Goetz, P. J. Bulk viscosity and compressibility measurement using acoustic spectroscopy. *The J. Chem. Phys.* **130**, 124519 (2009).

69. The HDF Group. Hierarchical Data Format, version 5 (1997-2017).

70. Xiao, S., Weiner, A. M. & Lin, C. A dispersion law for virtually imaged phased-array spectral dispersers based on paraxial wave theory. *IEEE J. Quantum Electron.* **40**, 420–426 (2004).

Acknowledgements

We thank Prof. Matthias Kirsch from the Department of Neurosurgery at the University Hospital Carl Gustav Carus for helpful discussions, the Advanced Light Microscopy Facility of the Max Delbrück Center for Molecular Medicine in the Helmholtz Association for technical support, the BIOTEC/CRTD Fish Facility for supplying the zebrafish specimens and the CMCB Light Microscopy Facility (partly funded by the State of Saxony and the European Fund for Regional Development - EFRE) for technical support and provision of the confocal fluorescence microscope. Financial support from the Alexander-von-Humboldt Stiftung (Humboldt-Professorship to J.G.) and the European Commission through the BIOPOL ITN (Marie Skłodowska Curie Action of the Horizon2020 program, grant agreement no 607350) is gratefully acknowledged.

Author contributions statement

R.S. realized the Brillouin microscope and evaluated the Brillouin measurements, S.M. prepared the zebrafish specimens and acquired and evaluated the brightfield and fluorescence images, R.S. and S.M. conducted the Brillouin measurements and wrote the manuscript with contributions from all authors, S.A. helped with sample preparation, C.M. and C.Z. supported the evaluation of the Brillouin measurements, R.S., S.M., J.C. and J.G. designed the experiments. All authors reviewed the manuscript.

Additional information

Accession codes The datasets generated during and/or analyzed during the current study are available from the corresponding author on reasonable request. **Competing financial interests** The authors declare no competing financial interests.